



# Na<sub>2</sub>WO<sub>4</sub>-tuned manganese ore as a high-effective redox catalyst for selective hydrogen combustion in the presence of methane and benzene

Xiaolin Ji<sup>a</sup>, Yanshuo Liu<sup>a</sup>, Jiamei Liu<sup>b</sup>, Junshe Zhang<sup>a,\*</sup>

<sup>a</sup> School of Chemical Engineering and Technology, Xi'an Jiaotong University, Xi'an, Shaanxi 710049, China

<sup>b</sup> Instrumental Analysis Center, Xi'an Jiaotong University, Xi'an, Shaanxi 710049, China

## ARTICLE INFO

### Keywords:

Methane dehydroaromatization  
Selective hydrogen combustion  
Redox catalyst  
Manganese ore  
Sodium tungstate

## ABSTRACT

Selective hydrogen combustion *in-situ* can break the thermodynamic limit of methane dehydroaromatization, which enhances the yield of aromatic hydrocarbons at a given operating temperature. In this study, sodium tungstate (Na<sub>2</sub>WO<sub>4</sub>) was loaded on manganese ore by incipient wetness impregnation, which improved the selectivity of hydrogen combustion dramatically. The selectivity of hydrogen combustion (the percentage of lattice oxygen species involved in hydrogen combustion) is 86% and 53% for Na<sub>2</sub>WO<sub>4</sub>-tuned and pristine manganese ore at 750 °C, respectively. Introducing Na<sub>2</sub>WO<sub>4</sub> causes a decrease in both the Mn(IV) fraction and oxygen vacancies in the surface layer as well as changes the crystal structure and the morphology of Mn ore. They are attributed to W ions substituting Mn ions, which makes benzene becomes more difficult to be activated compared with hydrogen at the metal oxide/Na<sub>2</sub>WO<sub>4</sub> interface.

## 1. Introduction

Among the direct transformations of methane (CH<sub>4</sub>) that is the main component of natural gas into liquid fuels and commodity chemicals, methane dehydroaromatization (MDA) is a very promising route because CH<sub>4</sub> is directly converted to aromatic compounds like benzene (C<sub>6</sub>H<sub>6</sub>) in the absence of any other reactants [1–4]. Currently, two major obstacles challenge the industrial implementation of MDA reaction, i.e., catalyst deactivation by coking and thermodynamic limitations [5]. Although lots of effort has been made to understand both the nature of active sites of ZSM-5-supported transition metals that are the very promising MDA catalysts and the carbon formation [1,6–9], the commercial MDA catalysts have yet developed. On the other hand, the thermodynamic barrier restricts the maximum yield of aromatics (benzene, toluene, and naphthalene) to be less than 35% at temperatures up to 800 °C. To overcome the latter, it has been suggested to remove hydrogen, one of MDA products, from the reaction zone [5,10–13]. Thus, MDA reaction is shifted toward the formation of aromatics, giving rise to an increase in aromatic yields.

Hydrogen removal can be achieved by carrying out MDA reaction in a catalytic membrane reactor, where hydrogen transfer is driven by the partial pressure difference cross the membrane. Caro and coworkers demonstrated that a U-shaped hydrogen-permeable hollow fiber

ceramic membrane improves the yield of aromatics by 47% (using CO<sub>2</sub> as the sweep gas) to 70% (using argon as the sweep gas) [12]. Serra and Kjøleth et al. showed that integration an electrochemical membrane that exhibits both proton and oxygen anion conductivity into an MDA reactor results in high aromatic yields and improves catalyst stability, which originate from the simultaneous extraction of hydrogen and injection of oxygen anions along the reactor. For these two types of membrane reactors, aromatics yield was below 12% [12,13]. Another approach to remove hydrogen from the reaction zone is selective hydrogen combustion (SHC), that means only hydrogen is oxidized to water under MDA reaction conditions. Hydrogen combustion not only favors the formation of aromatics but also alleviates coke formation by the *in-situ* generated water. Usually, oxygen can be brought to the reaction zone either through an oxygen-permeable membrane or by an oxygen transfer agent [5,10,11,13]. The main advantage of the latter over the former is that the transfer agent is packed together with the catalyst in a conventional fixed-bed reactor [10,11]. Xu et al. estimated that the latter strategy could improve the yield of aromatics up to > 40% that is much higher than those reported for membrane reactors [5,12,13]. Successful implementing the concept of coupling SHC with MDA in the conventional reactor resides in designing high-performance oxygen transfer agents, a.k.a. oxygen carriers (OCs).

Manganese-based oxygen carriers, such as MgMnO<sub>6</sub> and CaMnO<sub>3</sub>,

\* Corresponding author.

E-mail address: [jzhang08@xjtu.edu.cn](mailto:jzhang08@xjtu.edu.cn) (J. Zhang).

<https://doi.org/10.1016/j.apcatb.2022.121194>

Received 28 October 2021; Received in revised form 19 January 2022; Accepted 5 February 2022

Available online 8 February 2022

0926-3373/© 2022 Elsevier B.V. All rights reserved.

have been demonstrated to be excellent OCs for oxy-cracking of paraffins to produce olefins in a fixed-bed reactor [14–21]. In this scheme, lattice oxygen of OCs preferentially oxidize hydrogen, one product of either non-catalytic or catalytic cracking. As a result, a very small portion of hydrocarbons is oxidized under the oxy-cracking conditions, even though the oxygen carriers can oxidize hydrocarbons. In these respects, oxygen carriers can be called as redox catalysts that not only catalyze oxidations but also provide oxygen. These prior studies have clearly demonstrated that manganese-containing oxides could be promising redox catalysts for the scheme of coupling SHC with MDA in the traditional reactor. However, as far as we know, there is no reports on SHC over the aforementioned oxides in the presence of methane and aromatics.

Based on the thermodynamic analysis, oxidation of methane and benzene is thermodynamically more favorable than hydrogen oxidation at temperatures above 650 °C. Therefore, an ideal redox catalyst should have high selectivity toward hydrogen oxidation, extraordinary cycle stability, and excellent mechanical property. Additionally, from the viewpoint of industrial applications, the precursor of redox catalysts must be cheap and readily available. According to these criteria and previous reports, manganese ore — a natural aggregation of more than one minerals — could be a very promising candidate material. To improve its selectivity toward hydrogen combustion, we modified the manganese ore with sodium tungstate ( $\text{Na}_2\text{WO}_4$ ). The modification was achieved by incipient wetness impregnation (IWI). The catalysts were characterized by X-ray diffraction, X-ray photoelectron spectroscopy and electron paramagnetic resonance spectroscopy. The selective combustion was investigated by both temperature-programmed reaction and pulse techniques. Sodium tungstate significantly suppresses the oxidation of both hydrogen and benzene but it has a little effect on methane oxidation. After introducing  $\text{Na}_2\text{WO}_4$ , the temperatures at which hydrogen and benzene start to be oxidized increase by about 150 and 250 °C, respectively. For  $\text{Na}_2\text{WO}_4$ -tuned ore, around 86% of lattice oxygen is involved in hydrogen combustion at 750 °C. But, for the pristine ore, the percentage of lattice oxygen responsible for hydrogen combustion is about 53% at the same condition. At 750 °C, methane oxidation is ignorable. The introduction of  $\text{Na}_2\text{WO}_4$  not only changes the crystal structure of manganese oxide but also affects its surface property of the ore. These findings would inspire the rational develop of high-performance redox catalysts for selective oxidation of hydrogen.

## 2. Material and methods

### 2.1. Materials

Manganese ore was purchased from Hunan Qingchong Manganese Industry Co., sodium tungstate ( $\text{Na}_2\text{WO}_4 \cdot 2\text{H}_2\text{O}$ , 99.8%) and benzene ( $\text{C}_6\text{H}_6$ , 99%) were supplied by Sinopharm. All chemicals were used as received without further purification. D.I. water was provided by Tianyi Inc. Argon (Ar, 99.999%), oxygen ( $\text{O}_2$ , 99.8%), hydrogen ( $\text{H}_2$ , 99.999%), and methane ( $\text{CH}_4$ , 99.999%) which were purchased from Tengloung Inc.

### 2.2. Synthesis

Sodium tungstate was loaded onto the manganese ore by the IWI method. Typically, 1.0 g  $\text{Na}_2\text{WO}_4 \cdot 2\text{H}_2\text{O}$  was dissolved in 1.8 mL D.I. water, and the resulted solution was added dropwisely to 10.0 g of ore powders (>325 mesh) at room temperature under agitation. Afterward, the sample was kept under ambient conditions overnight, followed by drying at 120 °C for 12 h. Subsequently, it was calcined in a tubular furnace at 1000 °C for 12 h under continuous air flow. After calcination, the powder was pelletized, ground, and sieved to 200–450  $\mu\text{m}$  for testing. In the control experiment, the ore powders were treated by the same procedure expect for no sodium tungstate. The above two samples were referred to as W-Mn and P-Mn catalysts.

### 2.3. Characterization

X-ray diffraction (XRD) patterns were collected on a D/Max-R diffractometer (Shimadzu XRD 6100 laboratory) equipped with a Cu  $\text{K}\alpha$  radiation source ( $\lambda = 0.15406 \text{ nm}$ ). The working voltage and current were 40 kV and 30 mA, respectively. The sample was scanned at a 2 $\theta$  range of 10–90° with a rate of 5°/min.

The morphology of redox catalysts was examined by a GEMINI 500 field emission scanning electron microscopy (FE-SEM) that was operated at an accelerating voltage of 0.02–30 kV. The powders were dusted onto an adhesive conductive carbon belt attached to the sample holder, followed by blowing off the excess solid powder with nitrogen gas. Afterward, the sample stage was put into the sample chamber for observation.

X-ray photoelectron spectroscopy (XPS) measurements were carried out on an AXIS ULtrablde (Kratos) spectrometer using non-monochromatized Al  $\text{K}\alpha$  X-ray as the excitation source (1486 eV, 150 W). The sample was adhered to aluminum foil and then pressed into a 3  $\times$  3 mm square block under a pressure of 10 MPa, and it was excited by X-ray photons under ultra-high vacuum with a base pressure  $\sim 1 \times 10^{-8}$  mbar. Binding energies were calibrated with respect to the Si 2p photoelectron peak of aluminosilicate at 102.7 eV.

Electron paramagnetic resonance (EPR) spectroscopy was performed on a Bruker A300 spectrometer (X-band). About 50 mg sample (< 200  $\mu\text{m}$ ) was packed into the quartz EPR tube ( $\Phi_{\text{out}} = 4 \text{ mm}$ ), and it was heated to 1053 K under vacuum ( $P = 1.33 \text{ Pa}$ ), followed by pressurizing with oxygen to  $5.33 \times 10^4 \text{ Pa}$  and then keeping under these conditions for 30 min. This treatment was repeated once again. Subsequently, the tube was cooled down to room temperature under vacuum ( $P = 1.33 \text{ Pa}$ ) and then pressurized with oxygen to  $6.67 \times 10^4 \text{ Pa}$ . After maintaining at these conditions for 30 min, the tube was vacuumed to a base pressure of 1.33 Pa and then cooled down to 77 K before collecting EPR spectra. The microwave frequency and power were 9.85 GHz and 19 mW, respectively. The modulation amplitude and frequency were 1 G and 100 kHz, respectively.

### 2.4. Temperature-programmed reduction

Temperature-programmed reduction (TPR) was carried out on an in-house reaction unit (Fig. S1). The gaseous mixture was delivered by a gas panel equipped with mass flow controllers (ALICAT KM3100). The composition of the output stream was continuously monitored by a quadrupole mass spectrometer (Tilon LC-D200M). After loading 0.5 g of as-prepared catalyst particles (200–450  $\mu\text{m}$ ) into a quartz tube that was vertically placed inside an electric furnace (MTI OTF1200X) with a K-type thermocouple monitoring the furnace temperature, the tube was purged with 100 STP mL/min 5% $\text{H}_2$ /95%Ar gas mixture ( $\text{H}_2$ -TPR) or 5% $\text{CH}_4$ /95%Ar gas mixture ( $\text{CH}_4$ -TPR) until the signals became stable at RT. Afterwards, it was heated from RT to 900 °C at a ramping rate of 10 °C/min. In the case of benzene-TPR, benzene vapor was carried by argon (95 STP mL/min) passing through two bubblers in series which were filled with benzene. The first bubbler was kept at 30 °C and the second at 7 °C to ensure that argon was saturated. When hydrogen, methane and benzene were co-fed in the TPR experiment, benzene vapor was carried by 95 STP mL/min 5.26% $\text{H}_2$ /5.26% $\text{CH}_4$  /89.48% Ar gas mixture.

In the other two runs, the sample was kept at 750 °C for more than one hour after the temperature reached the above target value in 5% $\text{H}_2$ /95%Ar gas mixture (100 STP mL/min), and then the sample was cooled down to room temperature without switching off the gas mixture. Subsequently, the reduced sample was collected and stored in a glass vial at room temperature for further characterization.

### 2.5. Pulsing experiment

Pulsing experiment was performed on the above reaction unit. After loading 0.5 g of as-prepared catalyst particles (200–450  $\mu\text{m}$ ) into the

above reactor, pure argon (100 STP mL/min) was continuously fed to the reactor that was heated from RT to 200 °C. After the temperature reached the targeted value,  $H_2+CH_4+C_6H_6+Ar$  (1:1:1:10) gas mixture (5 consecutive pulses) was injected to the reactor through a 6-way valve with a 0.55 mL loop. The interval between each pulse was 7 min. Subsequently, the reactor was heated to 750 °C and the above injection was repeated. After that, the reactor was cooled down to 200 °C, the above injection was performed again. The amount of reactants injected to the reactor was the average value of ten pulses at 200 °C. The selectivity of hydrogen combustion ( $S_{H_2, combustion}$ ) was calculated from the following equation,

$$S_{H_2, combustion} = \frac{(0.5n_{CO} + n_{H_2, in}) - n_{H_2, out}}{(n_{H_2, in} - n_{H_2, out}) + 1.5n_{CO} + 2.5n_{CO_2}} \times 100\% \quad (1)$$

where  $n_{H_2, in}$  is the average amount of hydrogen injected (mol) to the reactor of ten pulses at 200 °C,  $n_{H_2, out}$  is the average amount of hydrogen unconsumed (mol) of five pulses at 750 °C,  $n_{CO}$  and  $n_{CO_2}$  is the average amount of CO and  $CO_2$  produced (mol) of five pulses at 750 °C, respectively. Herein, we assumed that methane oxidation is ignorable and benzene is both partially and totally oxidized.

## 2.6. Redox stability

After loading 0.15 g of as-prepared catalyst particles (200–450  $\mu m$ ) into the above reactor, it was heated from RT to 750 °C in pure Ar (100 STP mL/min). After the temperature reached the targeted value, argon was switched to a gas mixture of 5 vol% hydrogen balance with argon (100 STP mL/min). The reduction lasted for 18 min, followed by purging the reactor with pure argon (95 STP mL/min) for 5 min. Subsequently, argon was switched to a gas mixture of 5 vol% oxygen balance with argon (100 STP mL/min). The oxidation lasted for 18 min, followed by purging the reactor with pure argon (95 STP mL/min) for 3 min. Afterwards, the next redox cycle started.

## 3. Results

### 3.1. $H_2$ -TPR

Fig. 1 illustrates the  $H_2$ -TPR profiles of pristine and  $Na_2WO_4$ -tuned manganese ore. Hydrogen combustion starts at ca. 440 °C and maximizes around 560 °C over the former, whereas hydrogen oxidation begins at ca. 600 °C and maximizes around 860 °C over the later. The presence of  $Na_2WO_4$  not only suppresses hydrogen combustion but also changes the shape of TPR profile. After loading  $Na_2WO_4$ , it changes from a bell-shaped curve to a peak with two minor shoulders.

### 3.2. $CH_4$ -TPR

Because methane pyrolysis may occur at high temperature in the absence of catalysts, a control experiment was performed without packing manganese ore particles into the reactor and the result is shown in Fig. S2. As can be seen, both methane and hydrogen signals maintain unchanged at temperatures up to 900 °C. Therefore, methane pyrolysis is ignorable under the experimental conditions. As shown in Fig. 2, methane oxidation over both P-Mn and W-Mn catalysts is insignificant at temperatures below 800 °C. For the former, methane combustion is more important than the partial oxidation of methane; for the latter, methane combustion is inhibited but the partial oxidation is slightly promoted at temperatures above 800 °C. At temperatures up to 900 °C, no maximum in both CO and  $CO_2$  signals can be unambiguously identified.

### 3.3. $C_6H_6$ -TPR

In the absence of manganese ore, benzene pyrolysis occurs at

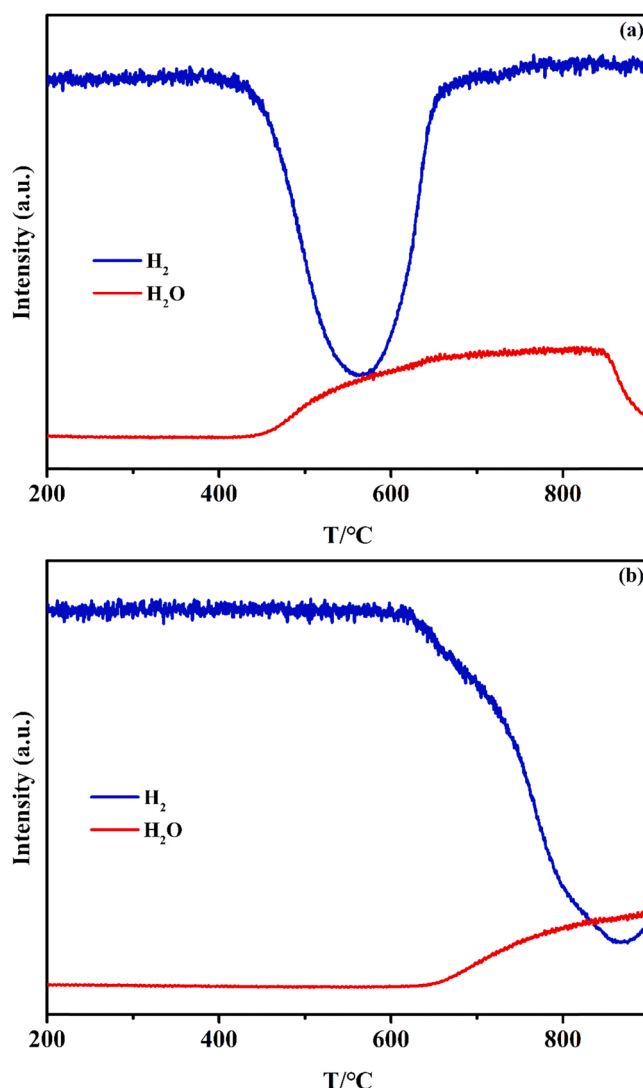


Fig. 1.  $H_2$ -TPR over P-Mn (a) and W-Mn (b):  $m_{cat.} = 0.5$  g,  $F_{Ar} = 95$  STP mL/min,  $F_{H_2} = 5$  STP mL/min, heating rate = 10 °C/min.

temperatures above 800 °C (Fig. S3). For P-Mn catalyst, benzene combustion and the partial oxidation of benzene start at ca. 500 and 650 °C, respectively; for W-Mn catalyst, the above two reactions begin at ca. 720 and 780 °C, respectively (Fig. 3). As illustrated in Fig. 3,  $CO_2$  and CO signals reach a maximum at ca. 770 and 800 °C over P-Mn catalyst, respectively; those signals maximize simultaneously at ca. 850 °C over W-Mn catalyst. Also, the amount of  $CO_2$  generated on W-Mn catalyst is much less than that on P-Mn catalyst. The total area of  $CO_2$  peaks at a temperature range of 200–900 °C for W-Mn and P-Mn catalysts is 0.60 and 2.34, respectively. Because the measurements were performed under the identical conditions, the area of peaks is proportional to the amount of  $CO_2$  produced. At temperatures below 750 °C, the amount of  $CO_2$  produced on W-Mn catalyst is only 2% of that on P-Mn catalyst. Another interesting observation is that there is a peak on the hydrogen profile over P-Mn catalyst but it is almost absent on that over W-Mn catalyst at temperatures below 820 °C.

### 3.4. $H_2+CH_4$ , $H_2+C_6H_6$ , and $H_2+CH_4+C_6H_6$ -TPR

Fig. 4 show the reduction of W-Mn catalyst by hydrogen and hydrocarbons mixture. Hydrogen combustion starts at ca. 600 °C and maximizes around 860 °C, which is independent of the type of hydrocarbons. Thus, hydrocarbons have little effect on the combustion of

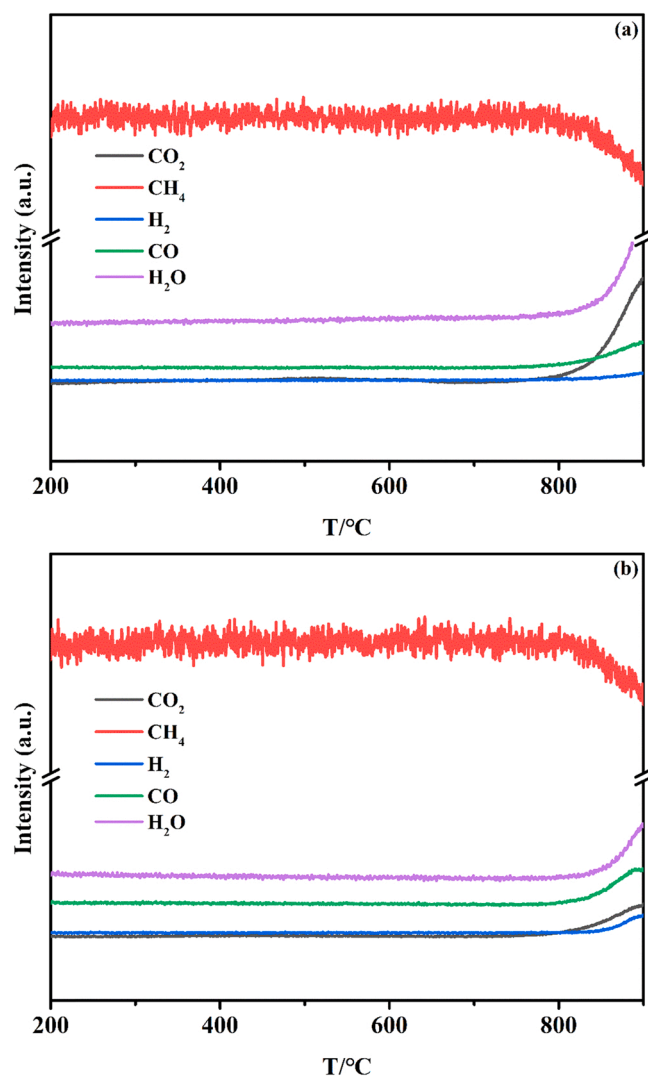


Fig. 2. CH<sub>4</sub>-TPR over P-Mn (a) and W-Mn (b):  $m_{cat.} = 0.5$  g,  $F_{Ar} = 95$  STP mL/min,  $F_{CH_4} = 5$  STP mL/min, heating rate = 10 °C/min.

hydrogen. As illustrated in Fig. 4, neither methane nor benzene consumption is significant at temperatures up to 900 °C. Upon combination of TRP results, we could conclude that W-Mn catalyst selectively burns hydrogen.

### 3.5. Selectivity of hydrogen combustion

Because MDA reaction is always carried out at a specific temperature, it is necessary to determine the selectivity of hydrogen combustion at the corresponding temperature. To evaluate the efficiency of hydrogen removal by selective combustion, a gas mixture of methane and main products of MDA was pulsed to a catalyst bed at 750 °C that is a typical MDA temperature. As can be seen in Table 1, the area of CH<sub>4</sub> peaks at 750 °C is very close to that at 200 °C, suggesting that the oxidation of methane is insignificant at 750 °C. For hydrogen and benzene, the area of peaks at 750 °C is less than that at 200 °C. In addition, the amount of CO<sub>2</sub> produced at 750 °C is 0.0535 μmol and that of CO produced is 0.0273 μmol. Therefore, the total oxidation is more important than the partial oxidation. Furthermore, we believe that CO and CO<sub>2</sub> predominantly stem from benzene oxidation at 750 °C. According to Eq. (1) and the data presented in Tables 1 and 2, the selectivity of hydrogen combustion is 86% and 53% for W-Mn and P-Mn catalysts, respectively. These findings clearly demonstrate that the

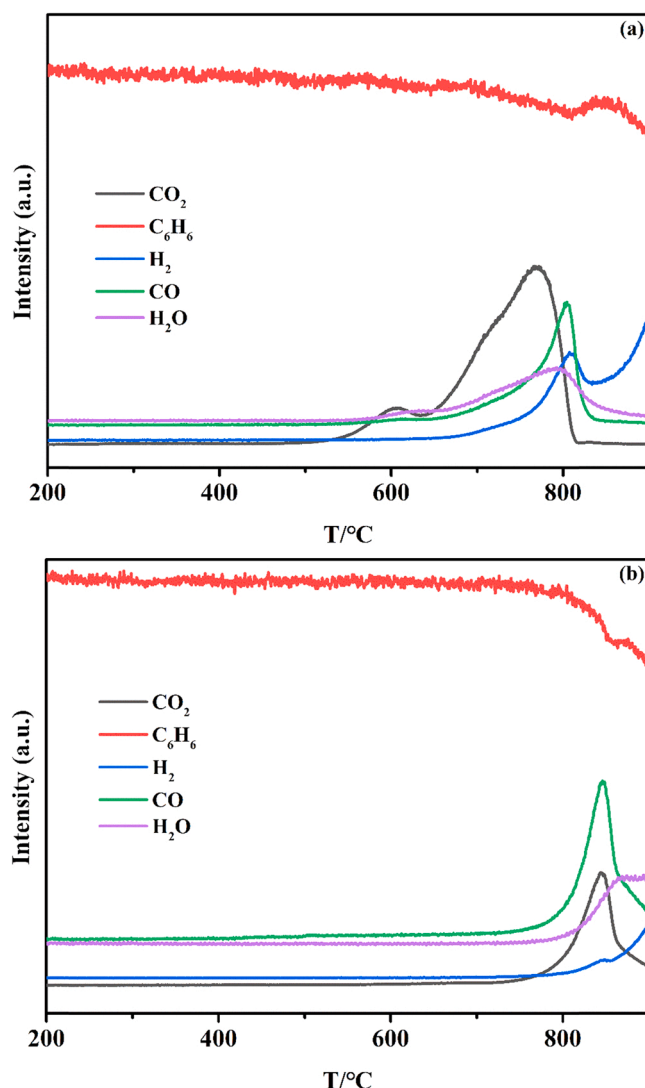


Fig. 3. C<sub>6</sub>H<sub>6</sub>-TPR over P-Mn (a) and W-Mn (b):  $m_{cat.} = 0.5$  g,  $F_{Ar} = 95$  STP mL/min,  $F_{C_6H_6} = 5$  STP mL/min, heating rate = 10 °C/min.

presence of sodium tungstate dramatically increases the selectivity of hydrogen combustion under the MDA conditions.

### 3.6. Stability

Besides high selectivity toward hydrogen combustion, the redox catalyst should have excellent cycling stability. That means the redox performance maintains unchanged over many cycles. To evaluate the cycling stability, W-Mn catalyst was subjected to 11 redox cycles at 750 °C and the results are presented in Fig. 5. Although the amount of water produced in the reduction step decreases slightly after 4 cycles, but it fluctuates around a specific value over the last 7 successive cycles. These observations demonstrate that W-Mn catalyst has good redox cyclability.

### 3.7. Properties of redox catalysts

The main Mn-containing crystalline phase of fresh and reduced W-Mn catalysts is cubic Mn<sub>2</sub>O<sub>3</sub> (Ia-3) and cubic MnO (Fm-3m), respectively (Fig. 6). For both samples, crystalline Na<sub>2</sub>WO<sub>4</sub> (cubic, Fd-3m) is detected at ambient conditions. It should be noted that sodium tungstate may exist in liquid state under typical MDA reaction temperatures, because the melting point of Na<sub>2</sub>WO<sub>4</sub> is 698 °C. For fresh P-Mn sample (Fig. S4),



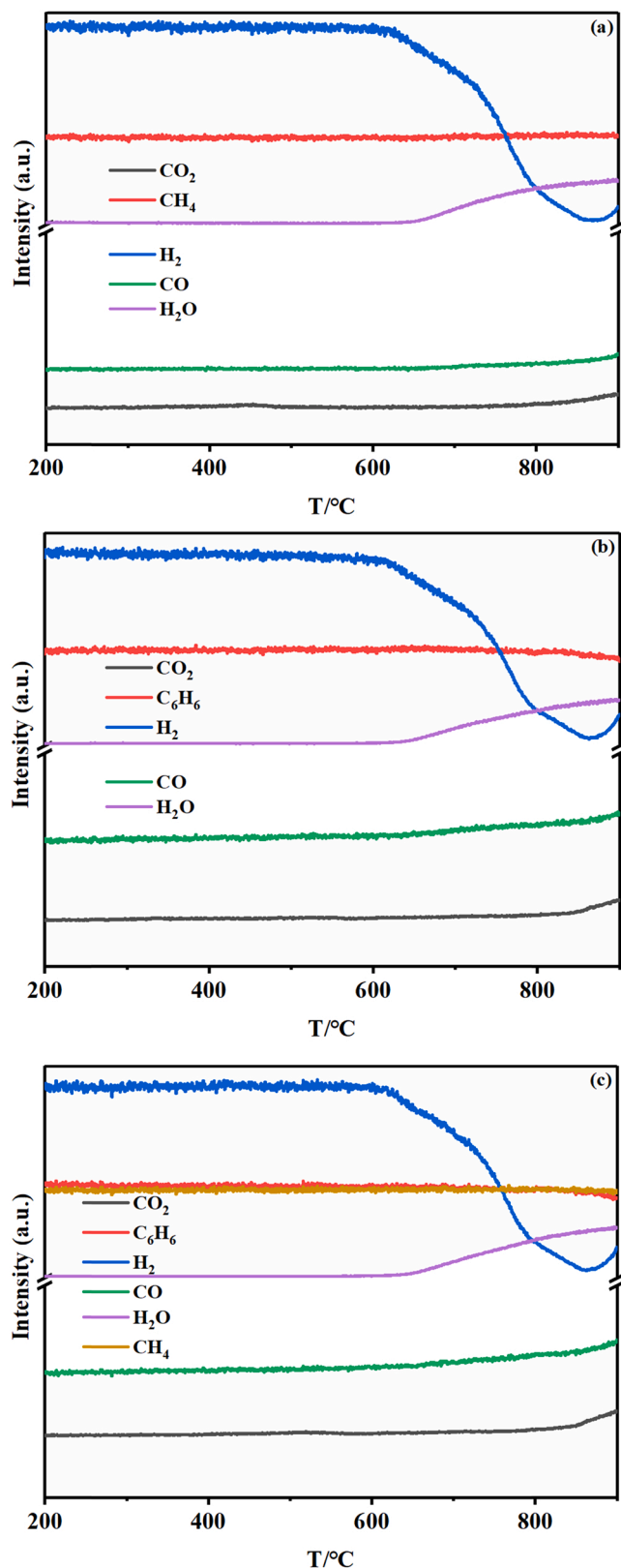


**Fig. 4.** (a)  $\text{H}_2$ ,  $\text{CH}_4$ -TPR over W-Mn:  $m_{\text{cat}} = 0.5$  g,  $F_{\text{Ar}} = 90$  STP mL/min,  $F_{\text{H}_2} = 5$  STP mL/min,  $F_{\text{CH}_4} = 5$  STP mL/min, heating rate =  $10^\circ\text{C}/\text{min}$ . (b)  $\text{H}_2$ ,  $\text{C}_6\text{H}_6$ -TPR over W-Mn:  $m_{\text{cat}} = 0.5$  g,  $F_{\text{Ar}} = 90$  STP mL/min,  $F_{\text{H}_2} = 5$  STP mL/min,  $F_{\text{C}_6\text{H}_6} = 5$  STP mL/min, heating rate =  $10^\circ\text{C}/\text{min}$ . (c)  $\text{H}_2$ ,  $\text{CH}_4$ ,  $\text{C}_6\text{H}_6$ -TPR over W-Mn:  $m_{\text{cat}} = 0.5$  g,  $F_{\text{Ar}} = 85$  STP mL/min,  $F_{\text{H}_2} = 5$  STP mL/min,  $F_{\text{CH}_4} = 5$  STP mL/min,  $F_{\text{C}_6\text{H}_6} = 5$  STP mL/min, heating rate =  $10^\circ\text{C}/\text{min}$ .

**Table 1**

Peak area of each component of 5 consecutive pulses injected to W-Mn catalyst bed at 200 and  $750^\circ\text{C}$ .

	Component	Pulse number				
		1 (a.u.)	2 (a.u.)	3 (a.u.)	4 (a.u.)	5 (a.u.)
200 °C (before)	$\text{H}_2$	7.48E-07	8.11E-07	8.37E-07	1.07E-06	8.55E-07
		07	07	07	06	07
	$\text{CH}_4$	3.82E-07	3.87E-07	3.83E-07	3.84E-07	3.86E-07
		07	07	07	07	07
	$\text{C}_6\text{H}_6$	6.18E-08	7.83E-08	8.75E-08	8.53E-08	9.08E-08
		08	08	08	08	08
750 °C	$\text{CO}$	1.35E-07	1.26E-07	1.31E-07	1.19E-07	1.30E-07
		07	07	07	07	07
	$\text{CO}_2$	3.26E-08	2.31E-08	8.59E-09	1.54E-08	1.67E-08
		08	08	09	08	08
	$\text{H}_2$	4.29E-07	4.75E-07	5.04E-07	5.07E-07	5.22E-07
		07	07	07	07	07
200 °C (after)	$\text{CH}_4$	3.81E-07	3.75E-07	3.74E-07	3.74E-07	3.76E-07
		07	07	07	07	07
	$\text{C}_6\text{H}_6$	5.00E-08	6.09E-08	7.17E-08	7.42E-08	7.63E-08
		08	08	08	08	08
	$\text{CO}$	1.32E-07	1.36E-07	1.33E-07	1.21E-07	1.29E-07
		07	07	07	07	07
750 °C	$\text{CO}_2$	4.24E-08	2.99E-08	2.58E-08	2.98E-08	2.32E-08
		08	08	08	08	08
	$\text{H}_2$	7.56E-07	8.30E-07	8.68E-07	8.68E-07	8.93E-07
		07	07	07	07	07
	$\text{CH}_4$	3.78E-07	3.78E-07	3.81E-07	3.84E-07	3.83E-07
		07	07	07	07	07
200 °C (after)	$\text{C}_6\text{H}_6$	4.76E-08	7.00E-08	7.96E-08	8.69E-08	9.02E-08
		08	08	08	08	08
	$\text{CO}$	1.13E-07	1.44E-07	1.21E-07	1.19E-07	1.33E-07
		07	07	07	07	07
	$\text{CO}_2$	3.20E-08	2.04E-08	1.17E-08	1.58E-08	1.48E-08
		08	08	09	08	08

**Table 2**

Peak area of each component of 3 consecutive pulses injected to P-Mn catalyst bed at 200 and  $750^\circ\text{C}$ .

	Component	Pulse number		
		1 (a.u.)	2 (a.u.)	3 (a.u.)
200 °C (before)	$\text{H}_2$	8.18E-07	8.54E-07	8.83E-07
	$\text{CH}_4$	4.02E-07	4.00E-07	3.97E-07
	$\text{C}_6\text{H}_6$	5.55E-08	6.72E-08	8.16E-08
	$\text{CO}$	1.26E-07	1.24E-07	1.34E-07
750 °C	$\text{CO}_2$	2.12E-08	1.62E-08	1.88E-08
	$\text{H}_2$	2.46E-07	2.61E-07	2.77E-07
	$\text{CH}_4$	4.05E-07	4.00E-07	4.02E-07
	$\text{C}_6\text{H}_6$	8.51E-08	1.03E-07	1.05E-07
200 °C (after)	$\text{CO}$	1.47E-07	1.43E-07	1.37E-07
	$\text{CO}_2$	1.99E-07	1.97E-07	1.93E-07
	$\text{H}_2$	8.36E-07	8.65E-07	8.80E-07
	$\text{CH}_4$	4.13E-07	4.14E-07	4.18E-07
750 °C	$\text{C}_6\text{H}_6$	1.29E-07	1.44E-07	1.54E-07
	$\text{CO}$	1.29E-07	1.44E-07	1.39E-07
	$\text{CO}_2$	2.41E-08	9.96E-09	1.18E-08

the main crystalline phase is tetragonal  $\text{Mn}_3\text{O}_4$  (I41/amd). Generally,  $\text{Mn}_3\text{O}_4$  forms when manganese oxide ( $\text{MnO}_x$ ) is heated at elevated temperatures, which is caused by the loss of lattice oxygen, and it would transform to  $\text{Mn}_2\text{O}_3$  when cooling down in air. Thus, the presence of  $\text{Na}_2\text{WO}_4$  affects the phase-transformation between  $\text{Mn}_3\text{O}_4$  and  $\text{Mn}_2\text{O}_3$ , most likely by promoting oxygen replenishment during the cooling step.

Fig. 7 illustrates the scanning electron micrographs of P-Mn and W-Mn catalysts. For these samples, individual particles tend to agglomerate together but the average size of agglomerates is much bigger for W-Mn catalysts than for P-Mn catalyst. Thus, introducing  $\text{Na}_2\text{WO}_4$  promotes agglomeration, most likely by acting as an adhesive at higher temperatures. As illustrated in Fig. S5, sodium tungstate appears to distribute homogeneously on both fresh and reduced catalysts. In addition, particle

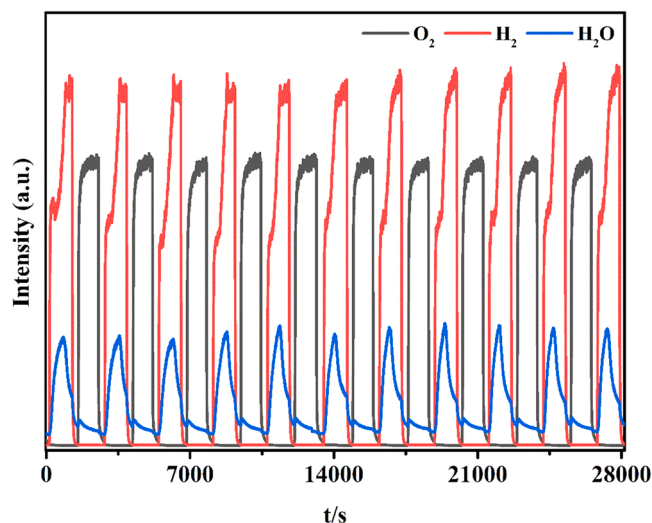


Fig. 5. W-Mn catalyst cycling stability testing:  $m_{cat.} = 0.15$  g,  $F_{Ar} = 95$  STP mL/min,  $F_{H_2} = 5$  STP mL/min,  $F_{O_2} = 5$  STP mL/min,  $750^\circ\text{C}$ .

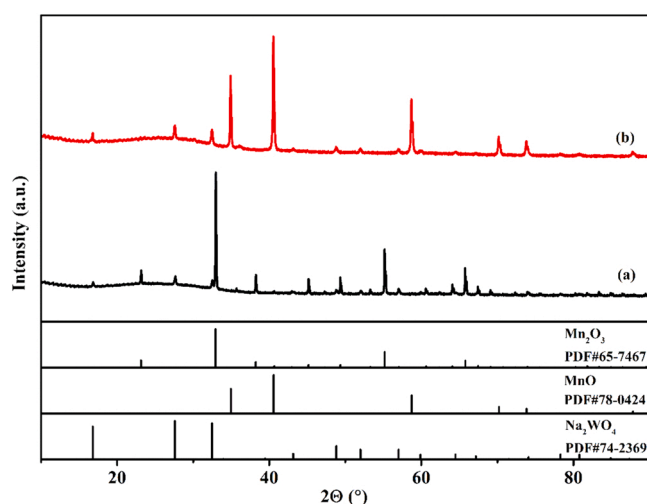


Fig. 6. XRD patterns of fresh W-Mn (a) and reduced W-Mn (b).

agglomerating is alleviated for reduced W-Mn catalyst.

The oxygen vacancy located in the surface layer of redox catalysts was characterized by EPR spectroscopy. For EPR measurements, dioxygen was used as the probe molecule that adsorbs on the oxygen vacancy sites, producing superoxide or peroxide species that can be detected by an EPR spectrometer. The first derivatives of the absorption spectra of fresh P-Mn and W-Mn catalysts are shown in Fig. 8. These two catalysts exhibit similar EPR spectral features (unstructured signals), but the  $g_{zz}$  component of  $\mathbf{g}$  tensor smaller for W-Mn catalyst than for P-Mn. This most likely because the charge of adsorption site increases in the presence of sodium tungstate [22–24]. The value of  $g_{yy}$  component is determined at the zero crossing of the derivative line shape, which corresponds to the maximum of the absorption spectrum. For fresh P-Mn and W-Mn catalysts, the  $g_{yy}$  value is 2.0035 and 2.0040, respectively. This suggests that sodium tungstate has a little effect on the magnetic field experienced by the free electron. Based on the double integration of the first-derivative line shape, the number of paramagnetic species can be estimated. By assuming that the measurement conditions (sample geometry, placement in the spectrometer, etc.) are identical and power saturation is absent, the change in the number of paramagnetic species after loading  $\text{Na}_2\text{WO}_4$  can be estimated. Our calculation shows that it decreases by 28%.

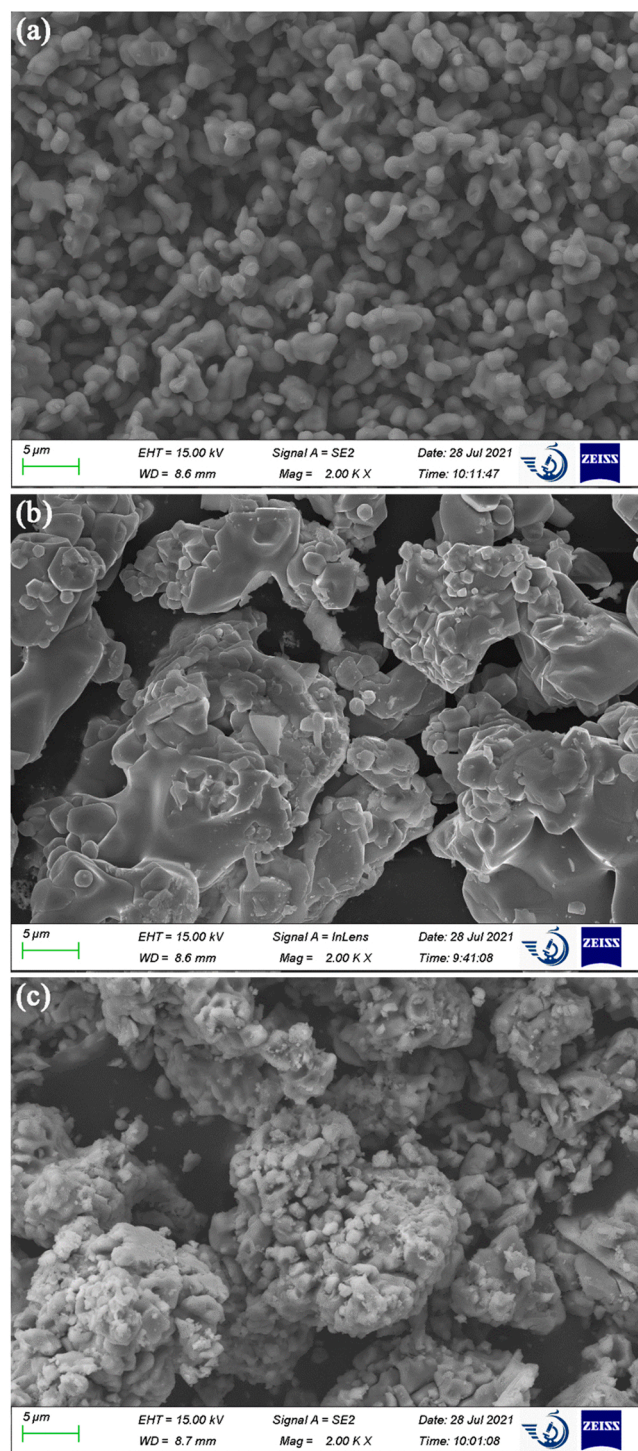


Fig. 7. SEM images of fresh P-Mn (a), fresh W-Mn (b), and reduced W-Mn (c).

The surface chemistry of redox catalysts was investigated by XPS. Fig. S6 shows full survey scans in a binding energy (BE) range of 0–1200 eV; the spectra suggest that manganese, silicon, and oxygen contribute significantly to the surface layer of P-Mn sample and the presence of sodium and tungstate along with the above three elements for W-Mn sample. The O 1s spectrum of W-Mn catalyst has a maximum ca. 532 eV, a distinct shoulder on the high binding energy side and another pronounced one on the low binding energy side. Thus, there exist at least three oxygen species in the surface layer. As shown in Fig. 9a, the spectrum is well fitted with three peaks:  $\text{O}^{2-}$  (lattice oxygen),  $\text{OH}^-$  and  $\text{H}_2\text{O}$  (physiosorbed, chemisorbed, or structurally bound water),

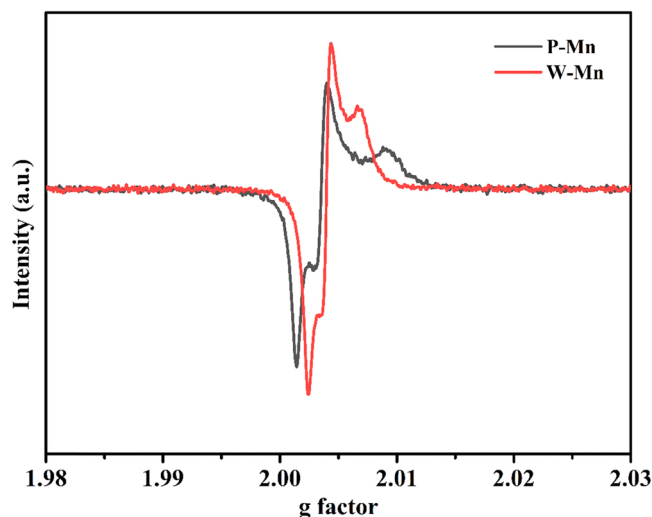


Fig. 8. EPR spectra of P-Mn and W-Mn.

centering at 529.96, 532.26 and 533.66 eV, respectively [25–28]. For P-Mn sample, the O 1s spectrum is also well fitted with the above three peaks. Table 3 lists fitted peak parameters, including BE, full width at half of maximum (FWHM), and intensity. As can be seen, the contribution of O<sup>2-</sup> to the O 1s spectrum increases after introducing Na<sub>2</sub>WO<sub>4</sub>. To determine the concentration of Mn(IV), Mn(III), and Mn(II) species in the surface layer, Mn 2p<sub>3/2</sub> spectra were fitted by multiple peaks whose parameters were derived from standards [25,29]. For one individual oxidation state, the peak parameters (BE, FWHM, and relative intensity) were fixed but change in the absolute intensity as a packet relative to another oxidation state was allowed. For P-Mn (W-Mn) catalyst, the atomic fractions of Mn(IV), Mn(III), and Mn(II) are 14.3 (0), 63.2 (76.7) and 22.5 (23.3)%, respectively.

#### 4. Discussion

Removal hydrogen from the reaction zone by selective hydrogen combustion intensities methane dehydroaromatization by both shifting the reaction equilibrium towards aromatics and providing heat to the exothermic reaction with minimized exergy loss. To maximum the yield of aromatics and carbon efficiency, it is required to minimize the oxidation of hydrocarbons, which can be achieved by using a redox catalyst. The redox catalyst donates its lattice oxygen when performing selective hydrogen combustion, and depleted oxygen is replenished by bringing the reduced catalyst into contact with air. Therefore, the use of a redox catalyst in selective hydrogen combustion circumvents the co-feed of gaseous oxidants and enables built-in reactive separation of oxygen from air. One key performance indicator of the redox catalyst is the selectivity of hydrogen combustion, whose definition has not been unified. For example, it was defined as either the fraction of lattice oxygen that reacts with hydrogen to generate water (yielding low SHC selectivity values) or the mole fraction of hydrogen combusted among all species that are oxidized by the lattice oxygen (yielding high SHC selectivity values) [20,21,30,31]. Herein, the former is adopted because it places emphasis on the conversion of lattice oxygen. For the pristine Mn ore,  $S_{H_2, combustion}$  is 53% at 750 °C when the feedstock contains hydrogen, methane, and benzene at equimolar fractions (0.05).

For the gas-solid oxidation reaction, the gaseous reactant first diffuses from the bulk gas phase to the solid surface. If the oxidation reaction of both hydrogen and hydrocarbons is controlled by the diffusion, then the selectivity of hydrogen combustion is mainly determined by the diffusivity of hydrogen and hydrocarbons. However, our observations clearly demonstrate that  $S_{H_2, combustion}$  is significantly affected by the properties of oxygen donating material (Figs. 6 and 9). Although the

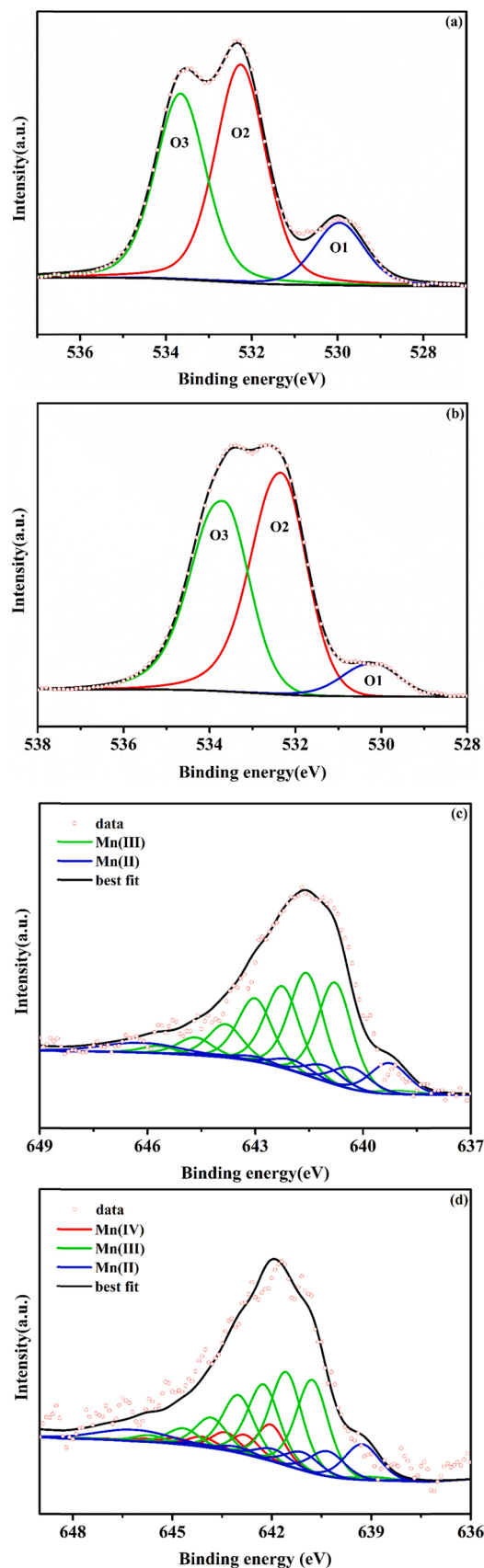


Fig. 9. XPS high-resolution O 1s spectra of W-Mn (a) and P-Mn (b) and Mn 2p<sub>3/2</sub> spectra of W-Mn (c) and P-Mn (d).



**Table 3**  
Fitted peak parameters for O 1s spectra.

	Name	Peak BE	FWHM eV	Area (a.u.)
P-Mn	O1	530.16	1.43	3569.3
	O2	532.33	1.43	24,088.85
	O3	533.67	1.43	21,651.57
W-Mn	O1	529.96	1.38	6829.73
	O2	532.26	1.38	23,925.29
	O3	533.66	1.38	20,411.26

crystal structure of manganese oxide changes after introducing sodium tungstate (Fig. 6), the bulk properties have a little effect on the selectivity of lattice oxygen toward hydrogen combustion but could affect its activity. Both the energy barrier of oxygen in the bulk metal oxide phase and the chemical potential of lattice oxygen are dependent on the bulk metal oxide phase; however, the gas-solid reactions are mostly confined to the surface and/or sub-surface regions of the solid. Therefore, we believe that the selectivity of hydrogen combustion is predominantly determined by the nature of solid surface, which can be tuned by introducing a promoter.

Generally, transition metal oxides exhibit high selectivity toward hydrogen combustion at low temperatures but the selectivity degrades as the operating temperature increases. This is because the activation energy is higher for the oxidation of hydrocarbons than for hydrogen combustion. At the typical MDA temperatures (700–800 °C), hydrogen and benzene compete for lattice oxygen (Figs. 1 and 3). To enhance the selectivity at high temperatures, the pristine Mn ore is modified with sodium tungstate that is an effective promoter for SHC redox catalysts [32]. For W-Mn catalyst, sodium tungstate atop Mn ore particles exists as an individual phase (Figs. 6 and 7). Introducing sodium tungstate causes the start temperatures of benzene oxidation and hydrogen combustion to high values (Figs. 1 and 3), which clearly suggests that the oxidation reaction is inhibited. These observations are also reported for other redox catalysts [17,33]. It was proposed that molten  $\text{Na}_2\text{WO}_4$  acts as an ion shuttle ( $\text{WO}_3 + \text{O}^{2-} \rightarrow \text{WO}_4^{2-} + \text{e}^-$ ,  $\text{WO}_4^{2-} + \text{H}_2 \rightarrow \text{WO}_3 + \text{H}_2\text{O} + \text{e}^-$ ) by which lattice oxygen migrate from the metal oxide to the  $\text{Na}_2\text{WO}_4$ /gas interface where the redox reactions occur, and vice versa [33]. If that is the case, then the activation energy of hydrogen combustion is weakly dependent on the nature of metal oxide/ $\text{Na}_2\text{WO}_4$  interface. For W-Mn catalyst, the apparent activation energy of hydrogen combustion, estimated from the TPR experiments with 3 different ramping rates (Fig. S7), is about 320 kJ/mol. This is almost 3.7 times as high as that over  $\text{Na}_2\text{WO}_4/\text{CaMnO}_3$  redox catalyst [17]. Even taking into the account the different methods used to estimate the apparent activation energy, the above pronounced difference cannot be solely explained by the aforementioned mechanism. According to that mechanism, the replenishment of lattice oxygen is achieved by  $\text{WO}_3 + 1/2\text{O}_2 + \text{e}^- \rightarrow \text{WO}_4^{2-}$ . However, no other tungstate-containing phases except for  $\text{Na}_2\text{WO}_4$  are detected in the reduced W-Mn catalyst (Fig. 6). Thus, we surmise that the oxidation reactions mainly take place at the metal oxide/ $\text{Na}_2\text{WO}_4$  interface.

After loading sodium tungstate, the atomic fraction of Mn(IV) in the surface layer of redox catalyst decreases to null. At the same time, the number of oxygen vacancies in that layer reduces by 28%. In general, doping with a low-valence dopant whose valence in its own stable oxide is lower than the valence of the cation it substitutes in the host oxide facilitates oxygen vacancy formation, and on the other hand doping with a high-valence dopant inhibits oxygen vacancy formation [34]. A high-valence dopant has excess electrons which can be donated to the cations in the host oxide, and thus reduces them. Therefore, the decrease in the atomic fraction of Mn(IV) and the number of oxygen vacancies in the surface layer is most likely due to surface doping, i.e., some W ions substituting Mn ions in the surface layer. Because  $\text{MnO}_2$  can change their oxidation state easily from 4+ to 3+ or 2+,  $\text{Mn}^{4+}$  can act as a strong Lewis acid that strongly binds Lewis bases such as H. In this regard, Mn

(IV) favors both hydrogen and benzene activation. Therefore, a decrease in the surface Mn(IV) concentration makes the redox catalyst a bad oxidant. But, it makes the redox catalyst more favorable toward selective hydrogen combustion. This may be because benzene becomes more difficult to be activated compared with hydrogen at the metal oxide/ $\text{Na}_2\text{WO}_4$  interface (Fig. 10). Tungsten ions substituting Mn ions in the surface layer changes the electronic structure of adsorption centers on which C and H adsorb, making them less favorable for benzene and hydrogen activation. This negative effect is attributed to either suppressing the intrinsic activity of the surface toward C–H bond scission or de-stabilizing the molecularly adsorbed state or both. Previous studies have demonstrated that the underlying O-ligand withdraws electron from the Pd atom, resulting in an attractive  $\text{CH}_4$ –Pd interaction that promotes C–H bond cleavage [35]. Therefore, it is reasonable to expect that an increase in the electron density around the Mn atoms most likely causes the activation of benzene and other hydrocarbons such as ethane and ethylene unfavorable.

## 5. Conclusions

In this work, manganese ore was explored as a potential redox catalyst that selectively oxidizes hydrogen in methane dehydroaromatization reaction system, which intensifies the process by both shifting the reaction equilibrium towards aromatics and providing heat to the exothermic process with minimized exergy loss. For the pristine Mn ore, the starting reduction temperature on the  $\text{H}_2$ -TPR profile is close that on the benzene-TPR profile but it is much lower than that on the  $\text{CH}_4$ -TPR profile. After introducing sodium tungstate, the starting reduction temperature increases significantly for hydrogen and benzene but changes slightly for methane. For a feed stream that contains equimolar fraction of  $\text{H}_2$ ,  $\text{CH}_4$  and benzene, the selectivity of hydrogen combustion (fraction of available lattice oxygen that reacts with hydrogen) at 750 °C is roughly correlated to the difference in the starting reduction temperature for hydrogen and benzene. The bigger is the latter, the higher is the former.

Introducing sodium tungstate causes a decrease in both the surface Mn(IV) concentration and oxygen vacancies in the surface layer as well as changes the crystal structure and the morphology of Mn ore. The change in the nature of surface layer comes from W ions substituting Mn ions, which makes benzene becomes more difficult to be activated compared with hydrogen at the metal oxide/ $\text{Na}_2\text{WO}_4$  interface. As a result, the selectivity of hydrogen combustion is enhanced.

Although  $\text{Na}_2\text{WO}_4$ -tuned Mn ore exhibits excellent selectivity toward hydrogen combustion and satisfactory cycling stability under the experimental conditions, the redox performance under the realistic conditions and long-term stability have not been investigated in detail. For an industrial process, the partial pressures of hydrogen and hydrocarbons are higher than those discussed here. It is worthwhile evaluating the effect of absolute and relative partial pressure of hydrogen on the selectivity in the future. Another interesting topic is optimizing the

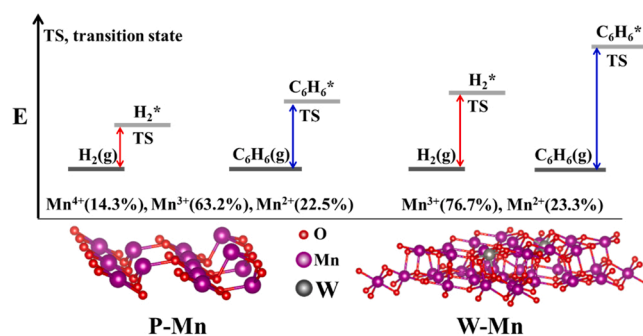


**Fig. 10.** Schematic illustration of both the surface of redox catalysts and the activation of hydrogen and benzene.



loading of sodium tungstate because our ongoing investigations reveal that its loading can be reduced further with no significant decline in the selectivity.

### CRedit authorship contribution statement

**Xiaolin Ji:** Methodology, Investigation, Data analysis, Writing – original draft. **Yanshuo Liu:** Investigation. **Jiamei Liu:** Resources, Software. **Junshe Zhang:** Conceptualization, Supervision, Data analysis, Funding acquisition, Writing – review & editing.

### Declaration of Competing Interest

The authors declare that they have no known competing financial interests or personal relationships that could have appeared to influence the work reported in this paper.

### Acknowledgments

This work was supported by the National Natural Science Foundation of China (No. 21978230, No. 22038011).

### Appendix A. Supporting information

Supplementary data associated with this article can be found in the online version at doi:10.1016/j.apcatb.2022.121194.

### References

- [1] D. Kiani, S. Sourav, Y.D. Tang, J. Baltrusaitis, I.E. Wachs, Methane activation by ZSM-5-supported transition metal centers, *Chem. Soc. Rev.* 50 (2021) 1251–1268.
- [2] U. Menon, M. Rahman, S.J. Khatib, A critical literature review of the advances in methane dehydroaromatization over multifunctional metal-promoted zeolite catalysts, *Appl. Catal. A* 608 (2020), 117870.
- [3] K.D. Sun, D.M. Ginosar, T. He, Y.L. Zhang, M.H. Fan, R.P. Chen, Progress in nonoxidative dehydroaromatization of methane in the last 6 years, *Ind. Eng. Chem. Res.* 57 (2018) 1768–1789.
- [4] Z.-G. Zhang, Process, reactor and catalyst design: towards application of direct conversion of methane to aromatics under nonoxidative conditions, *Carbon Resour. Convers.* 2 (2019) 157–174.
- [5] Z.W. Cao, H.Q. Jiang, H.X. Luo, S. Baumann, W.A. Meulenber, J. Assmann, L. Mleczko, Y. Liu, J. Caro, Natural gas to fuels and chemicals: improved methane aromatization in an oxygen-permeable membrane reactor, *Angew. Chem. Int. Ed.* 52 (2013) 13794–13797.
- [6] M. Caglayan, A.L. Paioni, E. Abou-Hamad, G. Shterk, A. Pustovarenko, M. Baldus, A.D. Chowdhury, J. Gascon, Initial carbon-carbon bond formation during the early stages of methane dehydroaromatization, *Angew. Chem. Int. Ed.* 59 (2020) 16741–16746.
- [7] N. Kosinov, A.S.G. Wijkema, E. Uslamin, R. Rohling, F.J.A.G. Coumans, B. Mezari, A. Parastaev, A.S. Poryvaev, M.V. Fedin, E.A. Pidko, E.J.M. Hensen, Confined carbon mediating dehydroaromatization of methane over Mo/ZSM-5, *Angew. Chem. Int. Ed.* 57 (2018) 1016–1020.
- [8] J. Gao, Y.T. Zheng, J.M. Jehng, Y.D. Tang, I.E. Wachs, S.G. Podkolzin, Identification of molybdenum oxide nanostructures on zeolites for natural gas conversion, *Science* 348 (2015) 686–690.
- [9] N. Kosinov, E.A. Uslamin, L.Q. Meng, A. Parastaev, Y.J. Liu, E.J.M. Hensen, Reversible nature of coke formation on Mo/ZSM-5 methane dehydroaromatization catalysts, *Angew. Chem. Int. Ed.* 58 (2019) 7068–7072.
- [10] Y. Zhang, H.Q. Jiang, A novel route to improve methane aromatization by using a simple composite catalyst, *Chem. Comm.* 54 (2018) 10343–10346.
- [11] C. Brady, B. Murphy, B.J. Xu, Enhanced methane dehydroaromatization via coupling with chemical looping, *ACS Catal.* 7 (2017) 3924–3928.
- [12] J. Xue, Y. Chen, Y.Y. Wei, A. Feldhoff, H.H. Wang, J. Caro, Gas to liquids: natural gas conversion to aromatic fuels and chemicals in a hydrogen-permeable ceramic hollow fiber membrane reactor, *ACS Catal.* 6 (2016) 2448–2451.
- [13] S.H. Morejudo, R. Zanon, S. Escolastico, I. Yuste-Tirados, H. Malerod-Fjeld, P. K. Vestre, W.G. Coors, A. Martinez, T. Norby, J.M. Serra, C. Kjolseth, Direct conversion of methane to aromatics in a catalytic co-ionic membrane reactor, *Science* 353 (2016) 563–566.
- [14] F. Hao, Y.F. Gao, J.N. Liu, R. Dudek, L. Neal, S. Wang, P.L. Liu, F.X. Li, Zeolite-assisted core-shell redox catalysts for efficient light olefin production via cyclohexane redox oxidative cracking, *Chem. Eng. J.* 409 (2021), 128192.
- [15] F. Hao, Y.F. Gao, L. Neal, R.B. Dudek, W.Y. Li, C.C. Chung, B. Guan, P.L. Liu, X. B. Liu, F.X. Li, Sodium tungstate-promoted CaMnO<sub>3</sub> as an effective, phase-transition redox catalyst for redox oxidative cracking of cyclohexane, *J. Catal.* 385 (2020) 213–223.
- [16] Y.F. Gao, S. Wang, F. Hao, Z.J. Dai, F.X. Li, Zeolite-perovskite composites as effective redox catalysts for autothermal cracking of n-hexane, *ACS Sustain. Chem. Eng.* 8 (2020) 14268–14273.
- [17] R.B. Dudek, Y. Tian, G.C. Jin, M. Blivin, F.X. Li, Reduction kinetics of perovskite oxides for selective hydrogen combustion in the context of olefin production, *Energy Technol.* 8 (2020), 1900738.
- [18] S. Yusuf, V. Haribal, D. Jackson, L. Neal, F.X. Li, Mixed iron-manganese oxides as redox catalysts for chemical looping-oxidative dehydrogenation of ethane with tailorable heat of reactions, *Appl. Catal. B* 257 (2019), 117885.
- [19] R.B. Dudek, X. Tian, M. Blivin, L.M. Neal, H.B. Zhao, F.X. Li, Perovskite oxides for redox oxidative cracking of n-hexane under a cyclic redox scheme, *Appl. Catal. B* 246 (2019) 30–40.
- [20] R.H. Dudek, Y.F. Gao, J.S. Zhang, F.X. Li, Manganese-containing redox catalysts for selective hydrogen combustion under a cyclic redox scheme, *AlChE J.* 64 (2018) 3141–3150.
- [21] L.M. Neal, S. Yusuf, J.A. Sofranko, F.X. Li, Oxidative dehydrogenation of ethane: a chemical looping approach, *Energy Technol.* 4 (2016) 1200–1208.
- [22] K. Sobanska, A. Krasowska, T. Mazur, K. Podolska-Serafin, P. Pietrzyk, Z. Sojka, Diagnostic features of EPR spectra of superoxide intermediates on catalytic surfaces and molecular interpretation of their g and a tensors, *Top. Catal.* 58 (2015) 796–810.
- [23] B. Bennett, Cryogenic electron paramagnetic resonance spectroscopy of flash-frozen tissue for characterization of mitochondrial disease, *J. Transl. Genet. Genom.* 4 (2020) 36–49.
- [24] S.A. Bonke, T. Risse, A. Schnegg, A. Brückner, In situ electron paramagnetic resonance spectroscopy for catalysis, *Nat. Rev. Methods Prim.* 1 (2021) 33.
- [25] H.W. Nesbitt, D. Banerjee, Interpretation of XPS Mn(2p) spectra of Mn oxyhydroxides and constraints on the mechanism of MnO<sub>2</sub> precipitation, *Am. Mineral.* 83 (1998) 305–315.
- [26] X.D. Zhang, X.T. Lv, F.K. Bi, G. Lu, Y.X. Wang, Highly efficient Mn<sub>2</sub>O<sub>3</sub> catalysts derived from Mn-MOFs for toluene oxidation: the influence of MOFs precursors, *Mol. Catal.* 482 (2020), 110701.
- [27] S.P. Mo, Q. Zhang, J.Q. Li, Y.H. Sun, Q.M. Ren, S.B. Zou, Q. Zhang, J.H. Lu, M. L. Fu, D.Q. Mo, J.L. Wu, H.M. Huang, D.Q. Ye, Highly efficient mesoporous MnO<sub>2</sub> catalysts for the total toluene oxidation: oxygen-vacancy defect engineering and involved intermediates using in situ DRIFTS, *Appl. Catal. B* 264 (2020), 118464.
- [28] M.C. Biesinger, B.P. Payne, A.P. Grosvenor, L.W.M. Lau, A.R. Gerson, R.S. Smart, Resolving surface chemical states in XPS analysis of first row transition metals, oxides and hydroxides: Cr, Mn, Fe, Co and Ni, *Appl. Surf. Sci.* 257 (2011) 2717–2730.
- [29] E.S. Ilton, J.E. Post, P.J. Heaney, F.T. Ling, S.N. Kerisit, XPS determination of Mn oxidation states in Mn (hydr)oxides, *Appl. Surf. Sci.* 366 (2016) 475–485.
- [30] J. Beckers, G. Rothenberg, Lead-containing solid “oxygen reservoirs” for selective hydrogen combustion, *Green Chem.* 11 (2009) 1550–1554.
- [31] J.H. Blank, J. Beckers, P.F. Collignon, G. Rothenberg, Redox kinetics of ceria-based mixed oxides in selective hydrogen combustion, *Chemphyschem* 8 (2007) 2490–2497.
- [32] R.B. Dudek, F.X. Li, Selective hydrogen combustion as an effective approach for intensified chemical production via the chemical looping strategy, *Fuel Process. Technol.* 218 (2021), 106827.
- [33] S. Yusuf, L. Neal, Z.H. Bao, Z.L. Wu, F.X. Li, Effects of sodium and tungsten promoters on MgMnO<sub>3</sub>-based core-shell redox catalysts for chemical looping-oxidative dehydrogenation of ethane, *ACS Catal.* 9 (2019) 3174–3186.
- [34] E.W. McFarland, H. Metiu, Catalysis by doped oxides, *Chem. Rev.* 113 (2013) 4391–4427.
- [35] S.D. Senanayake, J.A. Rodriguez, J.F. Weaver, Low temperature activation of methane on metal-oxides and complex interfaces: insights from surface science, *Acc. Chem. Res.* 53 (2020) 1488–1497.